Title

H2RSPET: a 0.5 mm resolution high-sensitivity small-animal PET scanner, a simulation study

Journal

Physics in Medicine and Biology, 66(6)

ISSN

0031-9155

Authors

Lai, Youfang
Wang, Qian
Zhou, Shiwei
et al.

Publication Date

2021-03-21

DOI

10.1088/1361-6560/abe558

Peer reviewed

HHS Public Access

Author manuscript

Phys Med Biol. Author manuscript; available in PMC 2022 March 09.

Published in final edited form as:

Phys Med Biol. ; 66(6): 065016. doi:10.1088/1361-6560/abe558.

H²RSPET: a 0.5 mm resolution high-sensitivity small-animal PET scanner, a simulation study

Youfang Lai[1], **Qian Wang**[2], **Shiwei Zhou**[1], **Zhaoheng Xie**[2], **Jinyi Qi**[2], **Simon R Cherry**[2], **Mingwu Jin**[1], **Yujie Chi**[1,*], **Junwei Du**[2,*]

[1]Department of Physics, University of Texas at Arlington, Arlington, TX 76019, United States of America

[2]Department of Biomedical Engineering, University of California at Davis, Davis, CA 95616, United States of America

Abstract

With the goal of developing a total-body small-animal PET system with a high spatial resolution of ~0.5 mm and a high sensitivity >10% for mouse/rat studies, we simulated four scanners using the graphical processing unit-based Monte Carlo simulation package (gPET) and compared their performance in terms of spatial resolution and sensitivity. We also investigated the effect of depth-of-interaction (DOI) resolution on the spatial resolution. All the scanners are built upon 128 DOI encoding dual-ended readout detectors with lutetium yttrium oxyorthosilicate (LYSO) arrays arranged in 8 detector rings. The solid angle coverages of the four scanners are all ~0.85 steradians. Each LYSO element has a cross-section of 0.44 × 0.44 mm^2 and the pitch size of the LYSO arrays are all 0.5 mm. The four scanners can be divided into two groups: (1) H^2RS110-C10 and H^2RS110-C20 with 40 × 40 LYSO arrays, a ring diameter of 110 mm and axial length of 167 mm, and (2) H^2RS160-C10 and H^2RS160-C20 with 60 × 60 LYSO arrays, a diameter of 160 mm and axial length of 254 mm. C10 and C20 denote the crystal thickness of 10 and 20 mm, respectively. The simulation results show that all scanners have a spatial resolution better than 0.5 mm at the center of the field-of-view (FOV). The radial resolution strongly depends on the DOI resolution and radial offset, but not the axial resolution and tangential resolution. Comparing the C10 and C20 designs, the former provides better resolution, especially at positions away from the center of the FOV, whereas the latter has 2 × higher sensitivity (~10% versus ~20%). This simulation study provides evidence that the 110 mm systems are a good choice for total-body mouse studies at a lower cost, whereas the 160 mm systems are suited for both total-body mouse and rat studies.

Keywords

PET; total-body; high-resolution; high-sensitivity

[*]Authors to whom any correspondence should be addressed. youfang.lai@mavs.uta.edu, Yujie.Chi@uta.edu and jwdu@ucdavis.edu.

1. Introduction

Small-animal positron emission tomography (PET) is a well-established nuclear medical imaging technique. With the aid of positron-emitting radionuclides, small-animal PET can image a wide range of molecular processes *in vivo* and hence is broadly used in the pre-clinical studies of pharmaceutical biodistributions and temporal disease progression (Hutchins et al 2008, Jones and Townsend 2017, Masopust et al 2017). It also serves as a critical platform for the development, validation, and characterization of the paradigms and protocols for clinical PET studies (Cherry 2006, Jones 2020). Several hundred small-animal PET scanners are now installed worldwide, and most academic medical research centers and pharmaceutical companies have access to and routinely use this technology (Myers 2001, Miyaoka and Lehnert 2020).

Key performance features of small-animal PET systems are spatial resolution, sensitivity, and count rate capability (Cherry et al 2012, Miyaoka and Lehnert 2020). Spatial resolution strongly affects the quantitative accuracy of PET imaging due to the partial volume effect, the single largest quantitative error in almost all small-animal PET studies. Sensitivity significantly impacts the quantitative precision due to the statistical uncertainties that are governed by Poisson counting statistics. Improving spatial resolution reduces the partial volume effect, thus improving accuracy. Increasing the scanner sensitivity increases the number of detected events thus increasing the precision of PET measurements. Increasing sensitivity also enables faster dynamic imaging, and improves the quality of temporal data that can feed into tracer kinetic models, such as the image-derived input functions from major arterial vessels (Lanz et al 2014, Huang et al 2019).

Since its early development in the 1990s (Cherry et al 1997), both academia and industry have put substantial effort to improve the spatial resolution and sensitivity of small animal PET (Schäfers et al 2005, Bao et al 2009, Yang et al 2016, Yamamoto et al 2016, Amirrashedi et al 2020, Gu et al 2020, Miyaoka and Lehnert 2020). However, none of the currently available small-animal PET scanners provide a combined performance of the theoretically achievable high spatial resolution (<0.5 mm) and high sensitivity (figure 1) (Levin and Hoffman 1999, Stickel and Cherry 2004). There have been three small animal PETs developed with ~0.5 mm resolution at the center of the field of view (FOV), however, they all suffer from low sensitivity. Specifically, the commercially available U-PET achieves ~0.5 mm resolution at the center of the FOV using a collimator, which adversely reduces its sensitivity to a very low level of ~0.3% (Miwa et al 2015, Miyaoka and Lehnert 2020). The PET system developed by Dr Yamamato and colleagues using lutetium yttrium oxyorthosilicate (LYSO) arrays with a pitch size of 0.42 mm and thickness of 5 mm has a resolution of ~0.6 mm and sensitivity of ~0.5% at the center of the FOV (Yamamoto et al 2016). The dedicated mouse brain PET developed by the University of California at Davis using lutetium oxyorthosilicate (LSO) arrays with a pitch size of 0.5 mm and thickness of 13 mm obtains a resolution of ~0.5 mm, but its sensitivity is only 0.7% at the center of the FOV (Yang et al 2016). The low sensitivities of these systems limit their applications to static studies or situations where the animals are subject to very high injected doses. Additionally, the small geometry of the latter two systems, diameter <61 mm and axial length <10 mm, further limits their primary applications to static mouse brain studies.

In this study, with a goal to design a small animal PET system with a resolution of ~0.5 mm and a high sensitivity >10% for total-body mouse/rat studies, we simulated four scanners with similar solid angles but different diameters (110 mm versus 160 mm), axial lengths (167 mm versus 254 mm) and crystal thicknesses (10 mm versus 20 mm) (table 1 and figure 2) using gPET, a graphics processing unit (GPU) based Monte Carlo (MC) package dedicated for PET simulation (Lai et al 2019). The performance in terms of spatial resolution and sensitivity of the four PET scanners was compared to find the optimal scanner for different applications.

2. Methods

2.1. Characteristics of the four small-animal PET scanners

The characteristics of the four scanners are shown in table 1. The four scanners were named H^2RS110-C10 PET, H^2RS110-C20 PET, H^2RS160-C10 PET, and H^2RS160-C20 PET. The schematics of the H^2RS110-C20 PET and H^2RS160-C20 PET are shown in figure 2. The four scanners are all composed of 128 dual-ended readout depth-of-interaction (DOI) encoding detector modules arranged in 8 detector rings. LYSO, the most widely used scintillator in state-of-the-art PET scanners, was selected because of its high light output, fast decay time, and high stopping power (Lewellen 2008, Du et al 2009). Compared to other DOI encoding detectors, such as detectors based on multi-layer crystals, crystal arrays with specially designed reflectors and monolithic crystals (Joung et al 2002, Kolb et al 2014, Lee and Lee 2015, Mohammadi et al 2019), the dual-ended readout detectors in combination with finely-segmented and thick crystals can simultaneously provide better DOI resolution, better spatial resolution and higher detector efficiency (Schmall et al 2012, Du et al 2018).

The H^2RS110-C10 PET and the H^2RS110-C20 PET were composed of 128 40 × 40 LYSO arrays with a pitch size of 0.5 mm, and both have a diameter of 110 mm and axial length of 167 mm. They are expected to provide high-resolution and high-sensitivity imaging across the whole body of the laboratory mice, which have a nose-to-anus-length of ~8–10 cm (Lin et al 2008). The H^2RS160-C10PET and the H^2RS160-C20 PET were composed of 128 60 × 60 LYSO arrays with a pitch size of 0.5 mm, and both have a diameter of 160 mm and axial length of 254 mm. They are supposed to provide high-resolution and high-sensitivity imaging across the whole body of the laboratory rats, which have a nose-to-anus-length of ~10–20 cm (Schellong et al 2013). The H^2RS110-C10 PET and the H^2RS160-C10 use LYSO arrays with a thickness of 10 mm, whilst the H^2RS110-C20 PET and the H^2RS160-C20 PET use LYSO arrays with a thickness of 20 mm.

2.2. Selection of the pitch size of the LYSO arrays

The pitch size of the LYSO array affects the resolution and the sensitivity of the PET scanners. The fundamental resolution at the center of the FOV of PET scanner can be roughly estimated using (Moses 2011, Cherry et al 2012)

$$\text{spatial resolution} = \sqrt{\left(\frac{\text{crystal size}}{2}\right)^2 + (\text{position range})^2 + (0.0022*\text{diameter})^2}. \quad (1)$$

Based on this formula, we estimated the resolution of the proposal PET scanners with diameters of 110 mm and 160 mm as a function of the crystal size, as shown in figure 3. Here, we assumed a 0.102 mm FWHM positron annihilation point distribution from the ^{18}F label source (Levin and Hoffman 1999). Better resolution can be obtained using smaller crystals (Stickel and Cherry 2004).

Reflectors are used to separate the LYSO elements, and optical glues are used to glue the reflector to the LYSO element in LYSO arrays. Both the reflectors and optical glue cannot detect gamma photons, hence they reduce the sensitivity of the PET scanner via reducing the fractional active area of the LYSO array. The lower the fractional active area, the lower the detection efficiency of the detector. The fractional active area of the crystal arrays can be estimated using

$$\text{fractional active area}(\%) = \left(\frac{\text{crystal size}}{\text{array pitch size}}\right)^2 \times 100\% . \quad (2)$$

Dual-ended readout detectors based on polished LYSO, Toray E60 with a thickness of 50 μm and 10 μm optical glue between crystal elements, can provide good crystal resolvability, energy resolution, and DOI resolution (Ren et al 2014, Du et al 2018). The fractional active area of these LYSO arrays is also shown in figure 3 (red line), which decreases when the crystal size reduces.

Based on our previous experimental results (Du et al 2018), LYSO arrays with a crystal size of 0.44 mm and pitch size of 0.5 mm were chosen in this work, which gives a good trade-off between the fractional active area of the LYSO array and the estimated resolution of the PET scanners (figure 3).

2.3. Simulations

Simulations of the four PET scanners were performed using gPET (Lai et al 2019). NEMA NU 4-2008, a standard for performance measurement of small animal PET systems, was followed to simulate the scanners and to report the resolution and sensitivity whenever possible. A ^{22}Na point source with an activity of 1500 Bq and a varying diameter of 0, 0.1, and 0.3 mm was used in all simulations. The source was embedded in an acrylic cube of 10.0 mm on each side. In the simulation, the energy resolution was set to be 16%, and the timing window was set to be 4 ns, based on experimental results (Du et al 2018).

Because we do not have the measured experimental energy resolutions for different crystal geometries, the 16% energy resolution was used to set the energy distribution of the gamma photons for all the four scanners in the simulation. Based on our previous experimental results, the energy resolutions of the four detector geometries will not have significant differences (Du et al 2018, 2019, Yang et al 2019).

2.3.1. Sensitivity—The sensitivities of the four PET scanners were simulated at different radial offsets and axial offsets, as shown in table 2. At each position, more than 10^6 coincidence events were collected. For each scanner, sensitivities obtained from the same

data set but using three energy windows of 150–750 keV, 250–750 keV, and 350–650 keV were compared.

2.3.2. Spatial resolution—The resolutions of the four PET scanners were simulated at different radial offsets and axial offsets, as shown in table 3. In the real experiment, a ^{22}Na point source with a diameter of no more than 0.3 mm in all directions is recommended to measure the spatial resolution following the NEMA NU 4-2008 standard. To investigate the effect of source size on the resolution, sources with three different diameters of 0, 0.1, and 0.3 mm were used in the simulation. In all simulations, an energy window of 250–750 keV was used to select events, and at each position, more than 10^6 coincidence events were collected.

In our simulation, the center of mass location (x_c, y_c and z_c) of the interaction of the annihilation photons in the LYSO array was recorded using

$$x_c = \frac{\sum_{i=1}^{N} x_i E_i}{\sum_{i=1}^{N} E_i}, \tag{3}$$

$$y_c = \frac{\sum_{i=1}^{N} y_i E_i}{\sum_{i=1}^{N} E_i}, \tag{4}$$

$$z_c = \frac{\sum_{i=1}^{N} z_i E_i}{\sum_{i=1}^{N} E_i}, \tag{5}$$

where the x_i, y_i, and z_i ($i = 1 \ldots N$) are the positions along axial, tangential, and radial directions for each interaction, respectively. E_i ($i = 1 \ldots N$) are the deposited energies blurred by energy resolution at each interaction, and N is the number of the interactions before one gamma photon deposited all its energy or escape from the crystal array. To model the effect of finite DOI resolution, the recorded position along the radial direction was added by a random displacement following a Gaussian distribution with the full width at half maximum (FWHM) being the DOI resolution (James et al 2009).

Although the filtered back projection (FBP) method is recommended by the NEMA NU 4-2008 protocol, the maximum likelihood expectation maximization (MLEM) algorithm is more popular for the reconstruction of data from most modern PET scanners (Hallen et al 2020). And MLEM is also more robust against noise and systematic inconsistencies than FBP (Nuyts et al 2001). Hence, the MLEM method with 12 iterations was used to reconstruct the images of the point source in our studies, and a voxel size of 0.04 × 0.04 × 0.04 mm^3 was used to make the voxel size at most one fifth of the finest resolution, following the NEMA NU 4-2008 standard. To avoid the artificially enhanced resolution measured using MLEM to fairly compare the four scanners with different geometries, a uniform background was used during our simulation. The contrast of point source to background in the reconstructed images was 10:1 (Gong et al 2016, Kyme et al 2017).

The spatial resolution of the reconstructed image along the radial, tangential, and axial direction was taken to be the FWHM of the point spread function (PSF) of the reconstructed point source along that direction. To calculate the PSF along one direction, the 3D reconstructed point source image was summed over the other two directions, following the NEMA NU 4-2008 standard. For example, to calculate the FWHM resolution along the axial direction, the reconstructed image was summed along the radial and tangential directions.

3. Results

3.1. Energy spectrum

Figure 4 shows the energy spectrum of the four scanners with the ^{22}Na source located at the center of the FOV of the scanners. Each spectrum was generated using 10^6 coincidence events. The energy spectrum of the H^{2}RS160-C20 PET had the fewest low-energy events, whilst the H^{2}RS110-C10 PET had the most. The percentages of events in a 250–750 keV energy window are 67.0%, 71.6%, 68.8%, and 74.7% for H^{2}RS110-C10, H^{2}RS110-C20, H^{2}RS160-C10, and H^{2}RS160-C20 PETs, respectively. This can be understood by the fact that the larger the detector size, the higher the probability that a photon can deposit all energy inside the detector through multiple interactions.

3.2. Sensitivity

Figure 5 shows the NEMA NU 4-2008 sensitivity of the four scanners obtained at different radial offsets and axial offsets using a 250–750 keV energy window to select events. At the center of the FOV, the sensitivities of the H^{2}RS110-C10 PET and the H^{2}RS110-C20 PET are 7.9% and 18.7%, respectively, and the sensitivities of the H^{2}RS160-C10PET and the H^{2}RS160-C20 PET are 8.9% and 22.0%, respectively. The sensitivities of the H^{2}RS110-C20 PET and the H^{2}RS160-C20 PET were more than 2 times higher than those of the H^{2}RS110-C10 PET and the H^{2}RS160-C10 PET, respectively. For a given crystal thickness, the scanner with a diameter of 160 mm had a slightly higher sensitivity than that with a diameter of 110 mm, which is due to the fact that the solid angles of the gap/dead space between crystals and detectors were smaller for the scanner with a larger diameter. The slightly lower ratio of low-energy events also contributed to higher sensitivity (figure 4).

Figure 6 shows the sensitivities of the four scanners along the central axis under three different energy windows. A higher sensitivity was obtained when a wider energy window was used, which is consistent with common expectations.

3.3. Spatial resolution

3.3.1. Spatial resolution versus radial offset and DOI resolution—Figure 7 shows the spatial resolution of the four scanners obtained at different radial offsets for varying DOI resolutions and at the axial center of the FOV using an ideal point source (diameter of 0 mm). The resolutions obtained at one-fourth of the axial FOV from the center of the axial FOV were similar to those obtained at the axial center of the FOV and omitted here for conciseness. From the resolution shown in figure 7, we made the following observations:

First, as expected, the radial resolution strongly depends on the source position and DOI resolution. However, the tangential and axial resolutions did not change significantly with source positions and DOI resolutions. A better radial resolution can be obtained if the scanner has a better DOI resolution. These are consistent with previous studies and suggest the importance of designing detectors with a good DOI resolution (Stickel and Cherry 2004, James et al 2009, Yoshida et al 2013).

Secondly, the spatial resolution of the scanners with the same diameter are similar if the scanners have the same DOI resolution.

Finally, for a given DOI resolution, the tangential and axial resolutions of the scanners with a diameter of 110 mm are better than those with a diameter of 160 mm for all radial offsets studied because non-collinearity is smaller for the detector ring with a smaller diameter (110 mm) than that with a larger one (160 mm). In contrast, the behavior of the radial resolution is quite different. The radial resolution is better for the scanners with a diameter of 110 mm than those with a diameter of 160 mm at the positions close to the center of the FOV, while the relation is reversed at the positions near the edge of the FOV. The reasons are detailed as follows. Aside from the non-collinearity effect, the radial resolution is affected by DOI as well. Under a given DOI resolution, the closer the source moves to the detector, the larger the DOI effect in the radial direction. Hence, moving from the center to the edge of the FOV, although the 160 mm systems start with a worse spatial resolution than the 110 mm systems, their resolution evolves with a smaller slop. Depending on the relative contribution of the DOI effect and the non-collinearity effect (Cherry et al 2012), the resolution trends of the two types of systems cross at a certain radial offset point. After this point, the radial resolution is worse for the 110 mm systems than for the 160 mm systems. Note that for perfect DOI resolution (0 mm), such a crossing phenomenon was not observed (top left of figure 7).

3.3.2. Spatial resolution of scanners with different DOI resolutions—Although substantial efforts have been devoted to improving the DOI resolution (Yoshida et al 2013, Ren et al 2014, Zatcepin et al 2020), the current experimentally achievable DOI resolution are ~1 and 2 mm for dual-ended readout PET detectors with 10 mm and 20 mm LYSO arrays, respectively (Du et al 2018, Yang et al 2019). Taking this into account, we compared the resolutions of the H^2RS110-C10 PET and the H^2RS160-C10 PET with 1 mm DOI resolution, and the H^2RS110-C20 PET and the H^2RS160-C20 PET with 2 mm DOI resolution. The results are shown in figure 8. As expected, for a given scanner diameter, scanners with 1 mm DOI resolution (H^2RS110-C10 PET and H^2RS160-C10 PET) have a better spatial resolution than those with 2 mm DOI resolution (H^2RS110-C20 PET and H^2RS160-C20 PET), especially for the radial resolution at positions away from the center of the FOV. This indicates that if high spatial resolution was the primary selection criteria, the H^2RS110-C10 PET and the H^2RS160-C10 PET would be a better choice.

3.3.3. Effect of the source diameter on the spatial resolution—Figure 9 shows the resolutions obtained using the ^{22}Na point source with three different diameters of 0, 0.1, and 0.3 mm for the scanners with DOI resolutions as discussed in section 3.3.2. The source size effects on the resolution obtained at other DOI resolutions exhibit similar trends

as the ones shown in figure 9 and are omitted here for conciseness. As can be seen from figure 9, the point source with a diameter of 0.1 mm has a negligible effect on the spatial resolutions, while the point source with a diameter of 0.3 mm had a significant effect on the spatial resolution. These results indicate that to measure the intrinsic resolution of the proposed PET scanners in a real experiment, the point source should have a size as small as possible and the widely used ^{22}Na point sources with diameters of 0.2–0.3 mm can lead to an overestimated resolution, i.e. an estimated resolution that is worse than the true resolution.

4. Discussions

The simulation results show that all four scanners can provide high spatial resolution and high sensitivity performance across their FOV and there is no clear-cut winner out of the four candidate designs. The best design choice depends on the specific applications and their requirements on resolution and sensitivity. Here, we recommend several choices among four designs for the following scenarios based on our current simulation study: (1) for studies that only use mouse models, the H^{2}RS110-C10 PET and the H^{2}RS110-C20 PET may be preferred, as these two scanners provide better spatial resolution (figures 6 and 7) at a lower cost, and (2) for rat studies, H^{2}RS160-C10 PET and the H^{2}RS160-C20 PET may be more appropriate as they provide a larger FOV to cover the entire rat body. The volume of LYSO needed for the H^{2}RS160-C20 PET and the H^{2}RS160-C20 would be 2.25 × of those for the H^{2}RS110-C10 PET and the H^{2}RS160-C10 PET, respectively.

The spatial resolutions of the scanners at the center of the FOV are all better than 0.5 mm. The radial resolution strongly depends on the radial offset and the DOI resolution. When the DOI resolution was better, the radial resolution was greatly improved. This indicates the importance of developing detectors with a high DOI resolution. The tangential and the axial resolutions were also affected by the DOI resolution, but with a much smaller magnitude (figure 6), which is consistent with previous studies (James et al 2009). Since the DOI resolution of 10 mm thick LYSO can be twice as good as that of 20 mm thick LYSO, the H^{2}RS110-C10 PET and the H^{2}RS160-C10 PET provide better resolution than the H^{2}RS110-C20 PET and the H^{2}RS160-C20 PET, respectively (figure 7).

The sensitivities at the center of FOV of the H^{2}RS110-C20 PET and the H^{2}RS160-C20 PET are ~20%, which are more than 2-fold higher than those of the H^{2}RS110-C10 PET and the H^{2}RS160-C10 PET (~10%) (figures 4 and 5). The sensitivities of the four proposed scanners are much better than currently available PET scanners with ~0.5 mm resolution (the UCD mouse brain PET, U-PET, and Yamamoto PET shown figure 1). The high sensitivity and larger FOV of the four scanners will also enable fast total-body dynamic imaging of mice and rats.

A ^{22}Na point source with a diameter smaller than 0.3 mm was recommended to measure the spatial resolution in NEMA NU 4-2008 protocol, and point sources with diameters of ~0.25 mm have been widely used (Kemp et al 2009, Yang et al 2016, Yamamoto et al 2016, Krishnamoorthy et al 2018). However, our simulation results show that to precisely measure the spatial resolution of scanners with an intrinsic resolution of ~0.5 mm, a point source with

a diameter smaller than 0.1 mm is preferred. Otherwise, the resolution will be overestimated (figure 9). To obtain the intrinsic resolution using sources with diameters larger than 0.1 mm, the intrinsic resolution can be estimated by subtracting the intrinsic resolution of the source, instead of the diameter or radius in quadrature from the measured resolution. We will study the intrinsic resolution of the source as a function of its diameter with the Monte Carlo in the future.

The inter-crystal and inter-detector scatter were not corrected in our studies, although the inter-crystal scatter correction can improve the spatial resolution and the inter-detector scatter correction can improve the sensitivity, respectively (Lee et al 2020). The inter-crystal scatter and inter-detector scatter were not corrected in our studies for two reasons. First, to design a high-resolution PET scanner, position-sensitive SiPMs (PS-SiPMs) are one attractive option (Schmall et al 2012, Du et al 2018). However, PS-SiPMs use center-of-gravity methods to calculate the gamma interaction position in the scintillator array, thus the inter-crystal scatter information is lost. Second, the inter-detector scatter was ignored to mimic the case that the readout electronics for each detector module work independently and in parallel, which can minimize the dead time of the readout electronics and increase the event processing rate of the electronics, hence, the peak noise equivalent count rate (NECR) will be maximized.

The NEMA image quality phantom and the micro Derenzo phantom were not investigated in our studies, because the four scanners had different diameters and our main focus is on comparing their sensitivity and spatial resolution. If the NEMA image quality phantom with its relatively small diameter of ~33 mm is used, the H^2RS110-C10 and the H^2RS110-C20 will give misleading results, as the H^2RS160-C10 and the H^2RS160-C20 provided a better resolution for positions far from the center (figures 7 and 8). The same is true for the Derenzo phantom. The resolution and sensitivity results from point sources at different locations already showed that there is no winner for all tasks, and that the best choice depends on the specific applications. In the future, before adopting any design, a simulation using custom phantoms that reflect a specific small-animal imaging task is necessary to assess whether the image quality can achieve the specific requirement of the small animal PET imaging applications.

The NECR was not investigated in our studies, which is due to that the NECR depends both on the performance of the detector modules and the deadtime of the readout electronics, and readout electronics for the proposed scanners is not available at this moment. We will conduct the NECR simulation when we further develop our readout electronics in the future. However, based on our previous experimental results, we expected that each of the proposed detector modules can handle higher than 100 000 events per second without performance degradation (Du et al 2018).

In our simulation, we chose to use LYSO crystals, which have similar properties as LSO crystals, such as high light output, fast decay time, and high stopping power (Lewellen 2008, Du et al 2009). Gadolinium aluminum gallium garnet (GAGG) has a higher light output than LYSO, and a dual-ended readout detector based on GAGG can provide a better DOI resolution. However, the stopping power of GAGG is lower than that of the LYSO,

hence, the inter-crystal and inter-detector scatter ratios are much higher in PET scanner with GAGG than that with LYSO (Lee et al 2020), making GAGG a less optimal choice for high-resolution PET than LYSO or LSO.

To build the proposed scanners, the most complex and difficult part is the LYSO arrays of $0.44 \times 0.44 \times 20$ mm^3 polished crystal pixels. During the past 10 years, working with our industrial collaborators, we have optimized the LYSO array fabrication methods, and it is now a routine to produce reliable scintillator arrays with crystal elements in the ~0.4×0.4 mm^2 cross-section range (Yang et al 2016, Du et al 2018, 2020, Kuang et al 2019). The reliability of the proposed scanners will also depend on the carefully designed electronics and gantries, which will not be a problem based on the currently available technologies (Yang et al 2016, Cherry et al 2018, Lv et al 2019).

5. Conclusions

With the goal of building a 0.5 mm resolution high-sensitivity small animal PET system for total-body mouse/rat studies, the resolution and sensitivity of four PET scanners were investigated using MC simulation and compared. The simulation study shows that the H^2RS110-C20 PET and H^2RS160-C20 PET have more than 2x the sensitivity of the H^2RS110-10 PET and H^2RS160-10 PET (~20% versus ~10%), while the latter two scanners provide a higher and more uniform spatial resolution across the FOV when taking the realistic DOI resolution into account. The H^2RS160-C10 PET and H^2RS160-C20 PET provide a larger FOV, which can be used for both total-body mouse and rat imaging. The H^2RS110-C10 PET and H^2RS110-C20 PET provide a smaller FOV, which is only suitable for total-body mouse imaging but provide a better resolution across the entire mouse body at a lower cost.

Acknowledgments

This work was funded by NIH grant R01 EB028806 and a Rising STARs award from University of Texas system.

Appendix

Table A1. The performance of small animal PET scanners shown in figure 1.

Name of scanner in figure 1	Volumetric resolution (mm^3)	Sensitivity (%)	Energy window (keV)	Timing window (ns)	DOI information	Reconstruction method	Reference
MicroPET	6	0.56	250-650	12	No	FBP	(Cherry et al 1997, Chatziioannou et al 1997)
MicroPET II	1.1	2.1	250-750	6	No	OSEM	(Yang et al 2004)
A-PET	8.7	3.6	250-665	7	No	FRP	(Surti et al 2005)
quadHIDAC32	1.2	1.5	350-650	Unknow	Yes	FBP	(Schäfers et al 2005)
GE VISTA	2.9	4	250-700	5/6.5/10 [*)]	Yes	FBP	(Wang et al 2006)

Name of scanner in figure 1	Volumetric resolution (mm^3)	Sensitivity (%)	Energy window (keV)	Timing window (ns)	DOI information	Reconstruction method	Reference
CdTe PET	0.4	4	Unknow	20	Yes	MLEM	(Ishii et al 2007)
F120	2.4	7.1	250-750	10	No	FBP	(Laforest et al 2007)
Inveon	5.4	7.2	350-650	3.43	No	FBP	(Kemp et al 2009)
nanoPET	1.2	7.7	250-750	5	No	FBP	(Szanda et al 2011)
ClearPET	7.6	4.7	250-750	Unknow	Yes	FBP	(Cañadas et al 2011)
PETBox4	3.4	18	150-650	20	No	MLEM	(Gu et al 2013)
nanoScan	1.8	8.4	250-750	5	No	FBP	(Nagy et al 2013)
LabPET-12	4.6	4.3	250-650	22	Yes	FBP	(Bergeron et al 2014)
DigiPET	0.34	0.3	400-650	20	No	MLEM	(España et al 2014)
ClairvivoPET	10	8.7	250-750	10	Yes	FBP	(Sato et al 2015)
U-PET	0.17	0.3	400-600	Unknow	No	OSEM	-(Miwa et al 2015, Miyaoka and Lehnert 2020)
UCD mouse brain	0.13	0.68	250-	60	Yes	MLEM	(Yang et al 2016)
Yamamoto PET	0.22	0.5	Unknow	16	No	FBP	(Yamamoto et al 2016)
Clip-on	0.47	4.7	250-750	12	Yes	OSEM	(Vrigneaud et al 2018)
β-CUBE	1	12.4	255-765	5	Yes	FBP	(Krishnamoorthy et al 2018)
HiPET	0.9	10.4	350-650	20/15/8 *	Yes	OSEM	(Gu et al 2020)
Albira PET	0.64	11	Unknow	Unknow	Yes	MLEM	(Gsell et al 2020)
SIAT aPET	0.55	11.9	350-750	6	Yes	OSEM	(Kuang et al 2020)

* Dual-layer crystal arrays with different crsytals were used.

References

Amirrashedi M, Zaidi H and Ay MR 2020 Advances in preclinical PET instrumentation PET Clin. 15 403–26 [PubMed: 32768368]

Bao Q, Newport D, Chen M, Stout DB and Chatziioannou AF 2009 Performance evaluation of the inveon dedicated PET preclinical tomograph based on the NEMA NU-4 standards J. Nucl. Med 50 401–8 [PubMed: 19223424]

Bergeron M, Cadorette J, Tétrault M-A, Beaudoin J-F, Leroux J-D, Fontaine R and Lecomte R 2014 Imaging performance of LabPET APD-based digital PET scanners for pre-clinical research Phys. Med. Biol 59 661–78 [PubMed: 24442278]

Cañadas M, Embid M, Lage E, Desco M, Vaquero JJ and Pérez JM2011NEMA NU 4-2008 performance measurements of two commercial small-animal PET scanners: ClearPET and rPET-1 IEEE Trans. Nucl. Sci 58 58–65

Chatziioannou AF, Cherry SR, Shao Y, Silverman RW, Meadors K, Farquhar TH, Pedarsani M and Phelps ME 1999 Performance evaluation of microPET: a high-resolution lutetium oxyorthosilicate

pet scanner for animal imaging J. Nucl. Med 40 1164–75 (https://jnm.snmjournals.org/content/40/7/1164) [PubMed: 10405138]

Cherry SR2006The 2006 Henry N. Wagner Lecture: of mice and men (and positrons)—advances in PET imaging technologyJ. Nucl. Med471735–45 (http://jnm.snmjournals.org/content/47/11/1735) [PubMed: 17079804]

Cherry SR, Jones T, Karp JS, Qi J, Moses WW and Badawi RD2018 Total-body PET: maximizing sensitivity to create new opportunities for clinical research and patient care J. Nucl. Med 59 3–12 [PubMed: 28935835]

Cherry SRet al.1997MicroPET: a high resolution PET scanner for imaging small animalsIEEE Trans. Nucl. Sci441161–6

Cherry SR, Sorenson JA and Phelps ME 2012 Physics in Nuclear Medicine E-Book (Amsterdam: Elsevier)

Du J, Bai X and Cherry SR 2020 A depth-encoding PET detector for high resolution PET using 1 mm SiPMs Phys. Med. Biol 65 165011 [PubMed: 32580180]

Du J, Bai X and Cherry SR 2019 Performance comparison of depth-encoding detectors based on dual-ended readout and different SiPMs for high-resolution PET applications Phys. Med. Biol 64 15NT03

Du J, Bai X, Gola A, Acerbi F, Ferri A, Piemonte C, Yang Y and Cherry SR 2018 Performance of a high-resolution depth-encoding PET detector module using linearly-graded SiPM arrays Phys. Med. Biol 63 035035 [PubMed: 29324437]

Du J, Wang Y, Zhang L, Zhou Z, Xu Z and Wang X2009 Physical properties of LYSO scintillator for NN-PET detectors 2009 2nd Int. Conf. on Biomedical Engineering and Informatics pp 1–5

España S, Marcinkowski R, Keereman V, Vandenberghe S and Holen RV2014 DigiPET: sub-millimeter spatial resolution small-animal PET imaging using thin monolithic scintillators Phys. Med. Biol 59 3405–20 [PubMed: 24888974]

Gong K, Cherry SR and Qi J 2016 On the assessment of spatial resolution of PET systems with iterative image reconstruction Phys. Med. Biol 61 N193–202 [PubMed: 26864088]

Gsell W. et al. 2020; Characterization of a preclinical PET insert in a 7 Tesla MRI scanner: beyond NEMA testing. Phys. Med. Biol. 65 :245016. [PubMed: 32590380]

Gu Z, Taschereau R, Vu NT, Prout DL, Lee J and Chatziioannou AF 2020 Performance evaluation of HiPET, a high sensitivity and high resolution preclinical PET tomograph Phys. Med. Biol 65 045009 [PubMed: 31935693]

Gu Z, Taschereau R, Vu NT, Wang H, Prout DL, Silverman RW, Bai B, Stout DB, Phelps ME and Chatziioannou AF 2013NEMA NU-4 performance evaluation of PETbox4, a high sensitivity dedicated PET preclinical tomograph Phys. Med. Biol 58 3791–814 [PubMed: 23666034]

Hallen P, Schug D and Schulz V 2020 Comments on the NEMA NU 4-2008 standard on performance measurement of small animal positron emission tomographs EJNMMI Phys. 7 12 [PubMed: 32095909]

Huang Q, Massey JC, Mińczuk K, Li J and Kundu BK2019 Non-invasive determination of blood input function to compute rate of myocardial glucose uptake from dynamic FDG PET images of rat heart *in vivo*: comparative study between the inferior vena cava and the left ventricular blood pool with spill over and partial volume corrections Phys. Med. Biol 64 165010 [PubMed: 31307015]

Hutchins GD, Miller MA, Soon VC and Receveur T 2008 Small animal PET imaging ILAR J 49 54–65 [PubMed: 18172333]

Ishii Ket al.2007First achievement of less than 1 mm FWHM resolution in practical semiconductor animal PET scannerNucl. Instrum. Methods Phys. Res. Sect. A576435–40

James SS, Yang Y, Bowen SL, Qi J and Cherry SR 2009 Simulation study of spatial resolution and sensitivity for the tapered depth of interaction PET detectors for small animal imaging Phys. Med. Biol 55 N63–74 [PubMed: 20023331]

Jones T. 2020; Total body PET imaging from mice to humans. Front. Phys. 8 :77.

Jones T and Townsend DW2017 History and future technical innovation in positron emission tomography J. Med. Imaging 4 011013

Joung J, Miyaoka RS and Lewellen TK2002 cMiCE: a high resolution animal PET using continuous LSO with a statistics based positioning scheme Nucl. Instrum. Methods Phys. Res. Sect. A 489 584–98

Kemp BJ, Hruska CB, McFarland AR, Lenox MW and Lowe VJ 2009NEMA NU 2-2007 performance measurements of the Siemens Inveon™ preclinical small animal PET system Phys. Med. Biol 54 2359–76 [PubMed: 19321924]

Kolb A, Parl C, Mantlik F, Liu CC, Lorenz E, Renker D and Pichler BJ 2014 Development of a novel depth of interaction PET detector using highly multiplexed G-APD cross-strip encoding Med. Phys 41 081916 [PubMed: 25086547]

Krishnamoorthy S, Blankemeyer E, Mollet P, Surti S, Holen RV and Karp JS 2018 Performance evaluation of the MOLECUBES β-CUBE—a high spatial resolution and high sensitivity small animal PET scanner utilizing monolithic LYSO scintillation detectors Phys. Med. Biol 63 155013 [PubMed: 29938684]

Kuang Zet al.2019Dual-ended readout small animal PET detector by using 0.5 mm pixelated LYSO crystal arrays and SiPMsNucl. Instrum. Methods Phys. Res. Sect. A9171–8

Kuang Z. et al. 2020; Design and performance of SIAT a PET: a uniform high-resolution small animal PET scanner using dual-ended readout detectors. Phys. Med. Biol. 65 :235013. [PubMed: 32992302]

Kyme AZ, Judenhofer MS, Gong K, Bec J, Selfridge A, Du J, Qi J, Cherry SR and Meikle SR 2017 Open-field mouse brain PET: design optimisation and detector characterisation Phys. Med. Biol 62 6207–25 [PubMed: 28475491]

Laforest R, Longford D, Siegel S, Newport DF and Yap J 2007 Performance evaluation of the microPET®—FOCUS-F120 IEEE Trans. Nucl. Sci 54 42–9

Lai Y, Zhong Y, Chalise A, Shao Y, Jin M, Jia X and Chi Y 2019 gPET: a GPU-based, accurate and efficient Monte Carlo simulation tool for PET Phys. Med. Biol 64 245002 [PubMed: 31711051]

Lanz B, Poitry-Yamate C and Gruetter R 2014 Image-derived input function from the Vena Cava for 18F-FDG PET studies in rats and mice J. Nucl. Med 55 1380–8 [PubMed: 24914058]

Lee MS and Lee JS 2015 Depth-of-interaction measurement in a single-layer crystal array with a single-ended readout using digital silicon photomultiplier Phys. Med. Biol 60 6495–514 [PubMed: 26247294]

Lee S, Kim KY, Lee MS and Lee JS 2020 Recovery of inter-detector and inter-crystal scattering in brain PET based on LSO and GAGG crystals Phys. Med. Biol 69 195005

Levin CS and Hoffman EJ 1999 Calculation of positron range and its effect on the fundamental limit of positron emission tomography system spatial resolution Phys. Med. Biol 44 781–99 [PubMed: 10211810]

Lewellen TK2008Recent developments in PET detector technologyPhys. Med. Biol53R287–317 [PubMed: 18695301]

Lin S-Y, Craythorn RG, O'Connor AE, Matzuk MM, Girling JE, Morrison JR and de Kretser DM2008 Female infertility and disrupted angiogenesis are actions of specific follistatin isoforms Mol. Endocrinol 22 415–29 [PubMed: 17932109]

Lv Y. et al. 2019; Mini EXPLORER II: a prototype high-sensitivity PET/CT scanner for companion animal whole body and human brain scanning. Phys. Med. Biol. 64 :075004. [PubMed: 30620929]

Masopust D, Sivula CP and Jameson SC2017 Of mice, dirty mice, and men: using mice to understand human immunology J. Immunol 199 383–8 [PubMed: 28696328]

Miwa K, Inubushi M, Takeuchi Y, Katafuchi T, Koizumi M, Saga T and Sasaki M2015 Performance characteristics of a novel clustered multi-pinhole technology for simultaneous high-resolution SPECT/PET Ann. Nucl. Med 29 460–6 [PubMed: 25894055]

Miyaoka RS and Lehnert A 2020 Small animal PET: a review of what we have done and where we are going Phys. Med. Biol 65 24TR04

Mohammadi I, Castro IFC, Correia PMM, Silva ALM and Veloso JFCA 2019 Minimization of parallax error in positron emission tomography using depth of interaction capable detectors: methods and apparatus Biomed. Phys. Eng. Express 5 062001

Moses WW2011Fundamental limits of spatial resolution in PETNucl. Instrum. Methods Phys. Res. Sect. A648S236–40 [PubMed: 21804677]

Myers R2001The biological application of small animal PET imagingNucl. Med. Biol28585–93 [PubMed: 11516702]

Nagy K, Tóth M, Major P, Patay G, Egri G, Häggkvist J, Varrone A, Farde L, Halldin C and Gulyás B 2013 Performance evaluation of the small-animal nanoScan PET/MRI system J. Nucl. Med 54 1825–32 [PubMed: 23990683]

Nuyts J, Michel C and Dupont P 2001 Maximum-likelihood expectation-maximization reconstruction of sinograms with arbitrary noise distribution using NEC-transformations IEEE Trans. Med. Imaging 20 365–75 [PubMed: 11403196]

Ren S, Yang Y and Cherry SR 2014 Effects of reflector and crystal surface on the performance of a depth-encoding PET detector with dualended readout Med. Phys 41 072503 [PubMed: 24989406]

Sato Ket al.2015Performance evaluation of the small-animal PET scanner ClairvivoPET using NEMA NU 4-2008 standardsPhys. Med. Biol61696–711 [PubMed: 26716872]

Schäfers KP, Reader AJ, Kriens M, Knoess C, Schober O and Schäfers M2005 Performance evaluation of the 32-Module quadHIDAC small-animal PET scanner J. Nucl. Med 46 996–1004 (http://jnm.snmjournals.org/content/46/6/996) [PubMed: 15937311]

Schellong K, Neumann U, Rancourt RC and Plagemann A 2013 Increase of long-term 'diabesity' risk, hyperphagia, and altered hypothalamic neuropeptide expression in neonatally overnourished 'small-for-gestational-age' (SGA) rats PLoS One 8 e78799 [PubMed: 24265718]

Schmall JP, Du J, Yang Y, Dokhale PA, McClish M, Christian J, Shah KS and Cherry SR 2012 Comparison of large-area position-sensitive solid-state photomultipliers for small animal PET Phys. Med. Biol 57 8119–34 [PubMed: 23172720]

Stickel JR and Cherry SR 2004 High-resolution PET detector design: modelling components of intrinsic spatial resolution Phys. Med. Biol 50 179–95

Surti S, Karp JS, Perkins AE, Cardi CA, Daube-Witherspoon ME, Kuhn A and Muehllehner G2005 Imaging performance of a-PET: a small animal PET camera IEEE Trans. Med. Imaging 24 844–52 [PubMed: 16011313]

Szanda I, Mackewn J, Patay G, Major P, Sunassee K, Mullen GE, Nemeth G, Haemisch Y, Blower PJ and Marsden PK2011 National electrical manufacturers association NU-4 performance evaluation of the PET component of the nanoPET/CT preclinical PET/CT scanner J. Nucl. Med 52 1741–7 [PubMed: 21969357]

Vrigneaud JM, McGrath J, Courteau A, Pegg R, Gomis AS-P, Camacho A, Martin G, Schramm N and Brunotte F 2018 Initial performance evaluation of a preclinical PET scanner available as a clip-on assembly in a sequential PET/MRI system Phys. Med. Biol 63 125007 [PubMed: 29762132]

Wang Y, Seidel J, Tsui BMW, Vaquero JJ and Pomper MG2006 Performance evaluation of the GE healthcare eXplore VISTA dual-ring small-animal PET scanner J. Nucl. Med 47 1891–900 (http://jnm.snmjournals.org/content/47/11/1891) [PubMed: 17079824]

Yamamoto S, Watabe H, Watabe T, Ikeda H, Kanai Y, Ogata Y, Kato K and Hatazawa J 2016 Development of ultrahigh resolution Si-PM-based PET system using 0.32 mm pixel scintillators Nucl. Instrum. Methods Phys. Res. Sect. A 836 7–12

Yang Q, Kuang Z, Sang Z, Yang Y and Du J 2019 Performance comparison of two signal multiplexing readouts for SiPM-based pet detector Phys. Med. Biol 64 23NT02

Yang Yet al.2016A prototype high-resolution small-animal PET scanner dedicated to mouse brain imagingJ. Nucl. Med571130–5 [PubMed: 27013696]

Yang Y, Tai Y-C, Siegel S, Newport DF, Bai B, Li Q, Leahy RM and Cherry SR 2004 Optimization and performance evaluation of the microPET II scanner for *in vivo* small-animal imaging Phys. Med. Biol 49 2527–45 [PubMed: 15272672]

Yoshida E, Tashima H, Hirano Y, Inadama N, Nishikido F, Murayama H and Yamaya T 2013 Spatial resolution limits for the isotropic-3D PET detector X'tal cube Nucl. Instrum. Methods Phys. Res. Sect. A 728 107–11

Zatcepin A, Pizzichemi M, Polesel A, Paganoni M, Auffray E, Ziegler SI and Omidvari N2020 Improving depth-of-interaction resolution in pixellated PET detectors using neural networks Phys. Med. Biol 65 175017 [PubMed: 32570223]

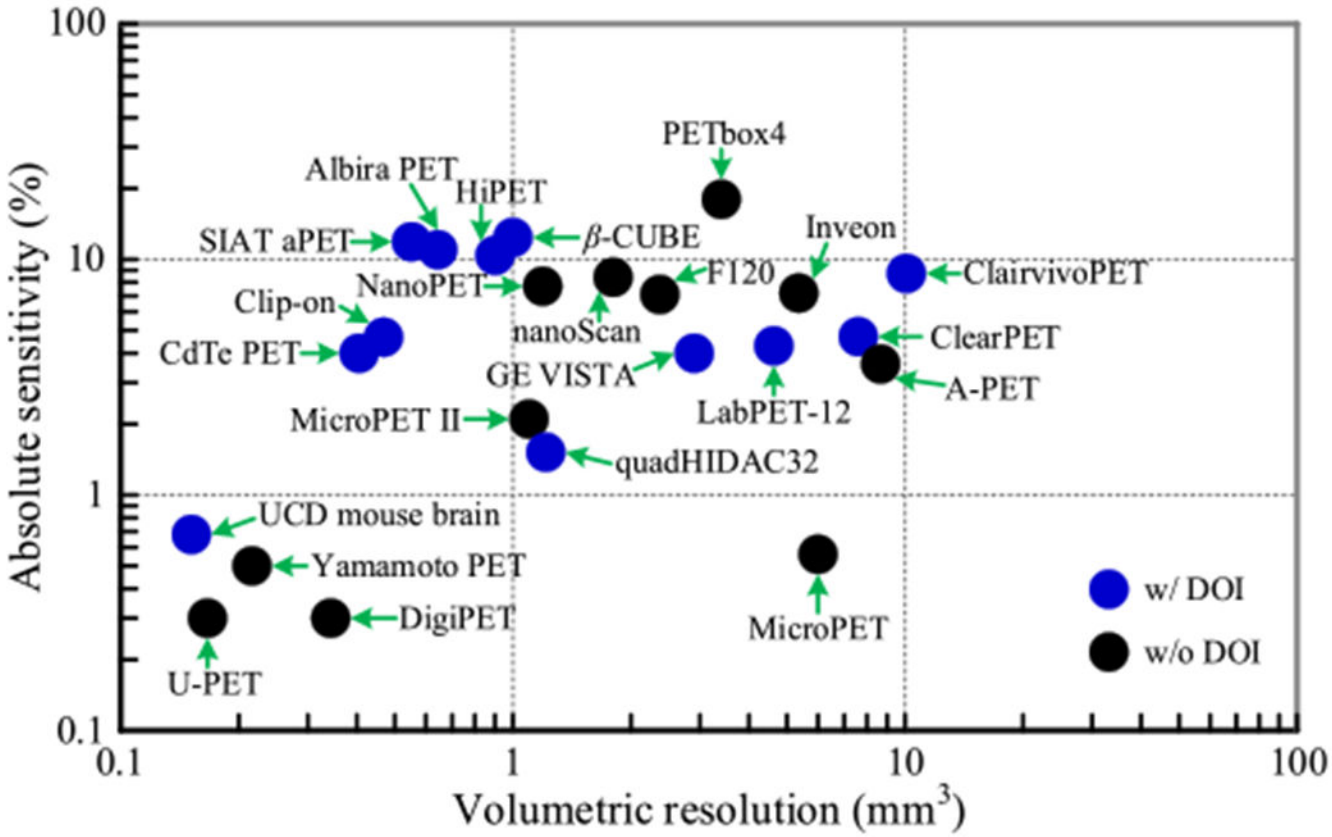

Figure 1.

The performance of small animal PET scanners. Only scanners with published results were selected. The resolution and sensitivity values obtained at the center of the scanners were used. Because the resolutions in the axial, tangential, and axial directions were different, volumetric resolution, which is the product of the resolution in each of the three directions, was used. The resolutions of the scanners were obtained using different reconstruction methods, which could slightly affect the resolution comparison, but did not affect the sensitivities. The sensitivities of the scanners were obtained using different energy windows. Detailed performance of the scanners including reconstruction method are shown in table A1. (Chatziioannou et al 1999, Yang et al 2004, Surti et al 2005, Schäfers et al 2005, Wang et al 2006, Ishii et al 2007, Laforest et al 2007, Kemp et al 2009, Cañadas et al 2011, Szanda et al 2011, Gu et al 2013, Nagy et al 2013, Bergeron et al 2014, España et al 2014, Sato et al 2015, Yamamoto et al 2016, Krishnamoorthy et al 2018, Vrigneaud et al 2018, Lv et al 2019, Gu et al 2020, Gsell et al 2020, Kuang et al 2020, Miyaoka and Lehnert 2020.)

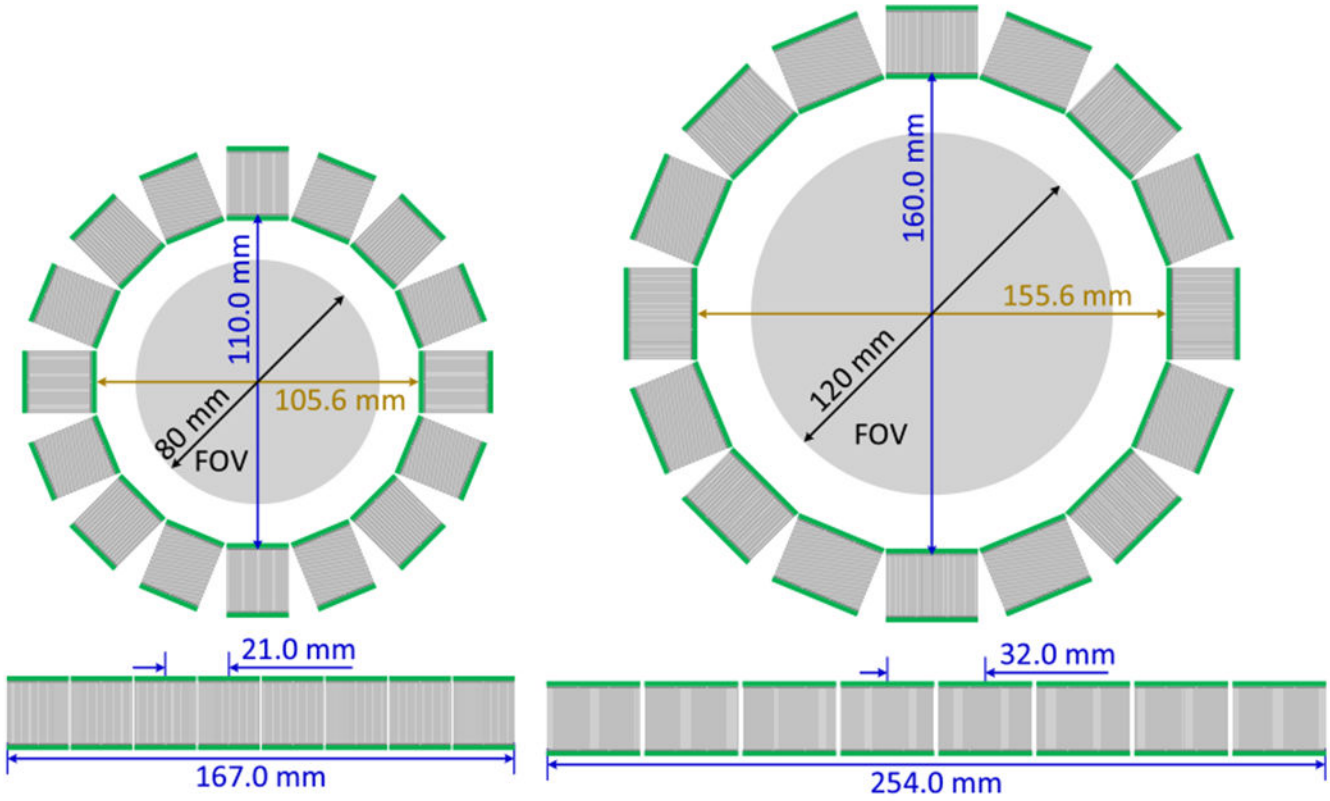

Figure 2.

The schematics of (left) the H^2RS110-C20 PET and (right) the H^2RS160-C20 PET. The H^2RS110-C10 PET and the H^2RS160-C10 PET have the same diameter and axial length as those of the H^2RS110-C20 PET and the H^2RS160-C20 PET, respectively. C10 denotes a crystal thickness of 10 mm, and C20 of 20 mm.

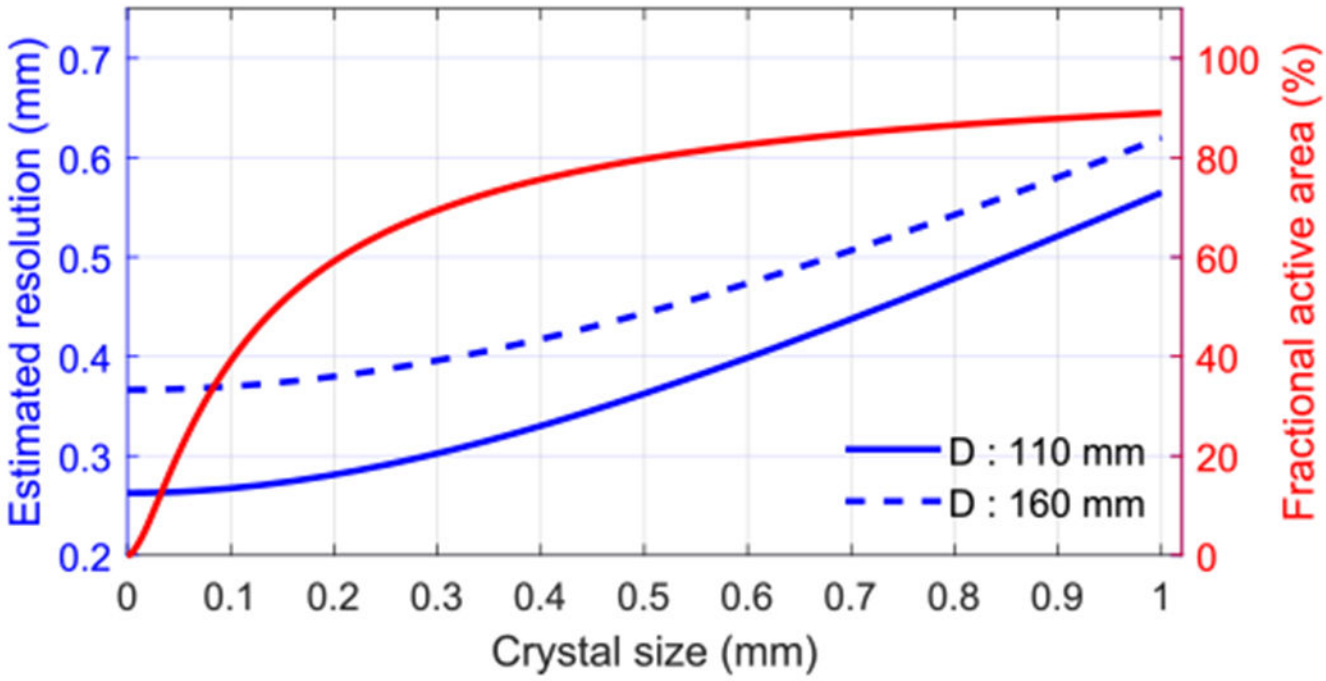

Figure 3.

The estimated spatial resolution at the center of FOV for two scanners with ring diameters of 110 mm and 160 mm. The red line shows the fractional active area of the LYSO array with 50 μm Toray E60 reflector and 10 μm optical glue.

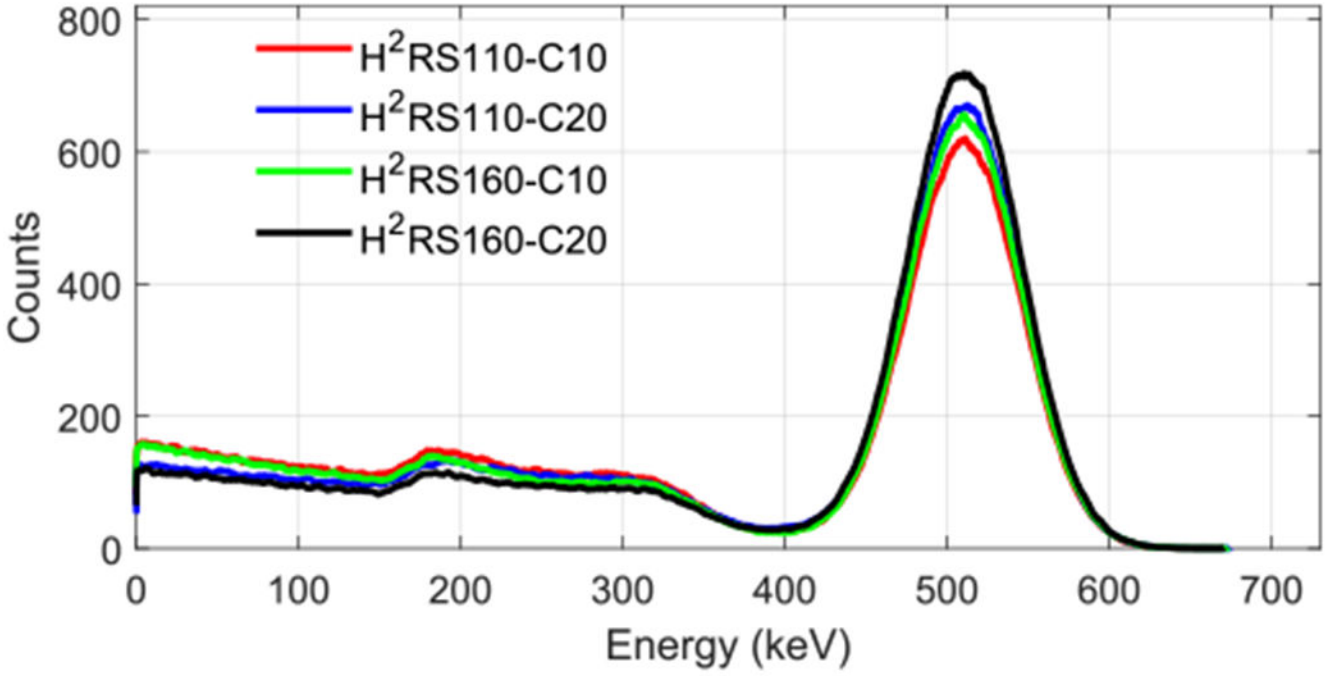

Figure 4.

Energy spectra for the four scanners obtained by locating the ^{22}Na source at the center of FOV. For each energy spectrum, 10^6 coincidence events were used.

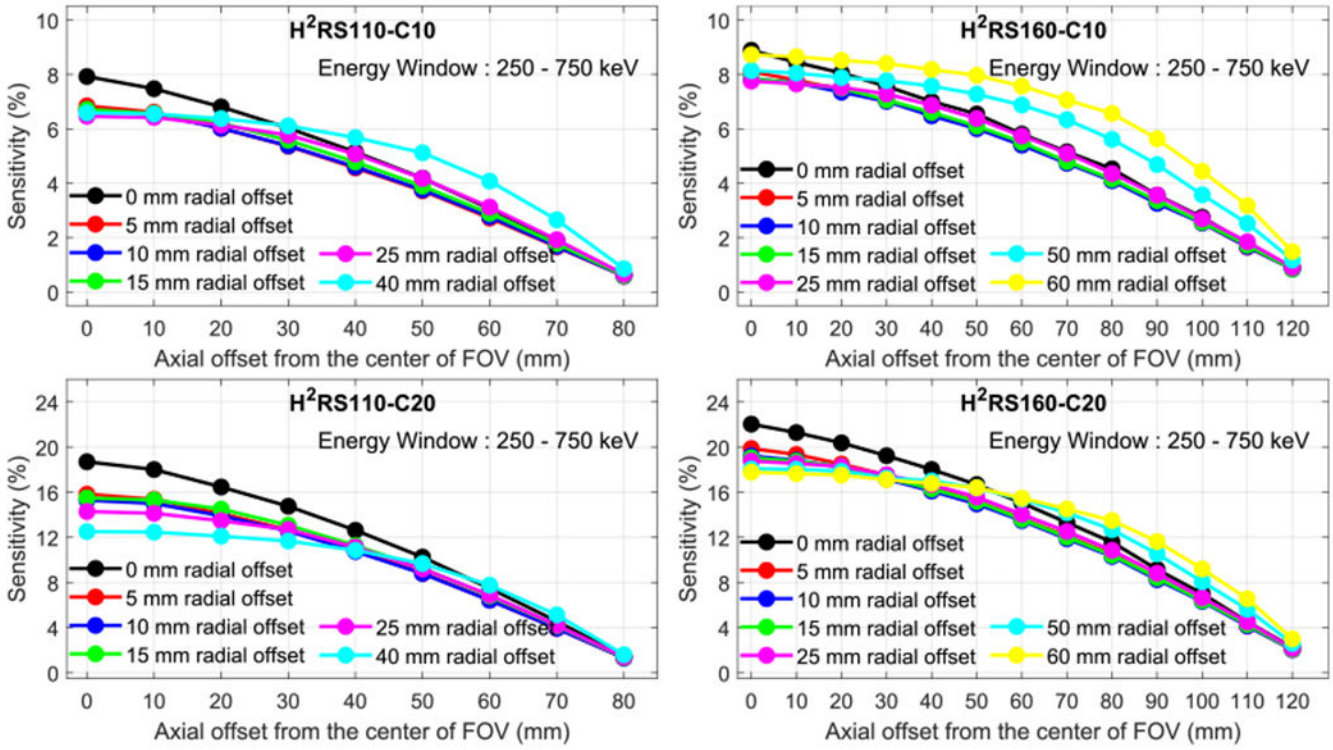

Figure 5.

Sensitivity versus radial offset and axial offset for (left top) H^2RS110-C10, (left bottom) H^2RS110-C20, (right top) H^2RS160-C10 and (right bottom) H^2RS160-C20. A 250–750 keV energy window was used to select events.

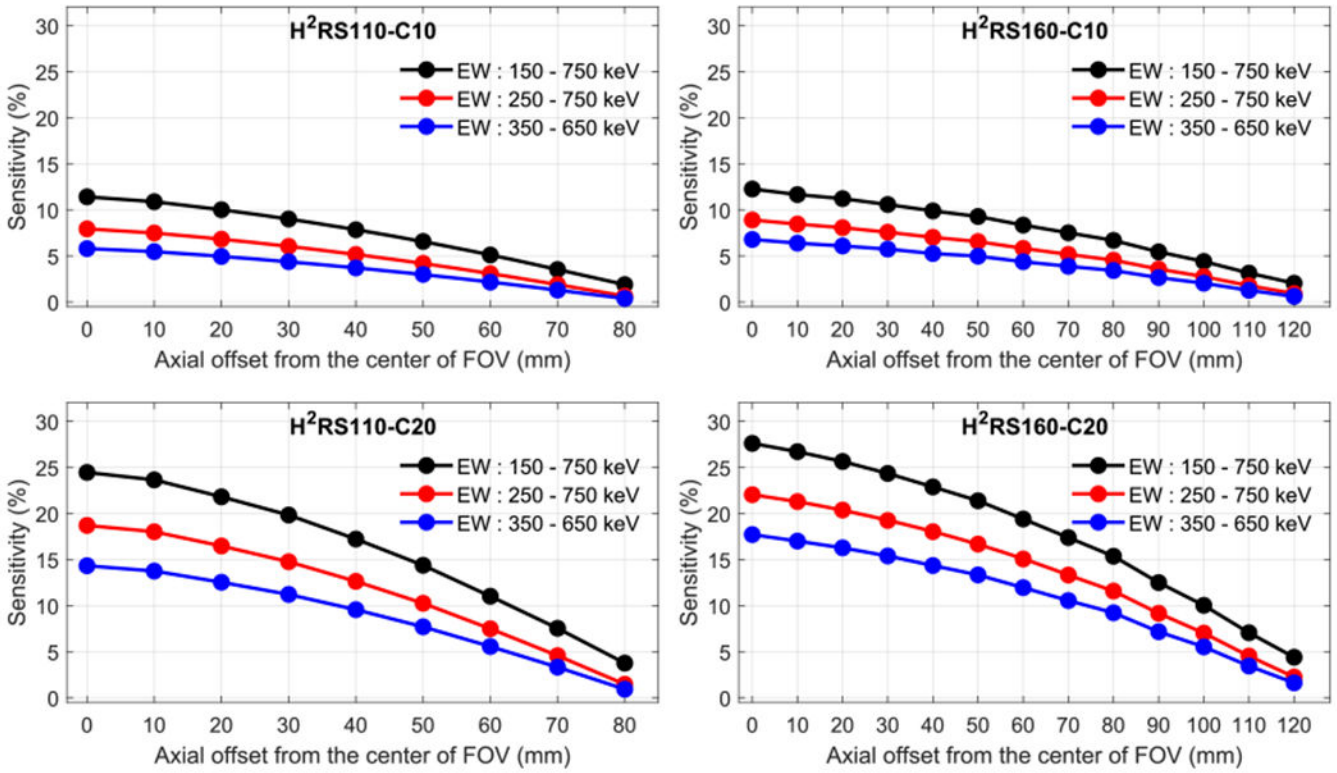

Figure 6.

Sensitivity along center axial obtained using three different energy windows. H^2RS110-C10 (left top), H^2RS110-C20 (left bottom), H^2RS160-C10 (right top) and H^2RS160-C20 (right bottom).

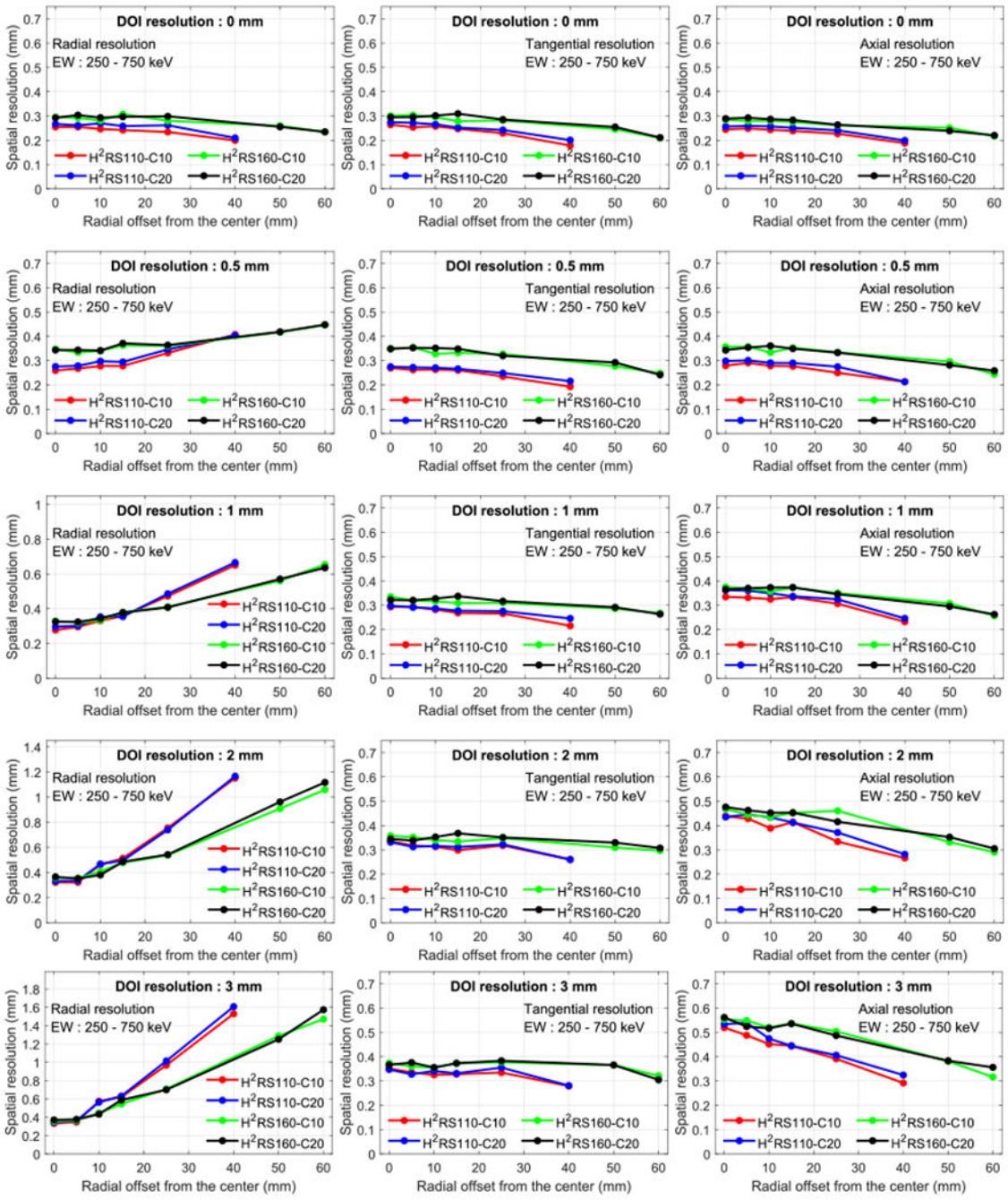

Figure 7.

Radial (left column), tangential (middle column) and axial (right column) resolution versus radial offset and DOI resolution. A 250–750 keV energy window was used to select events.

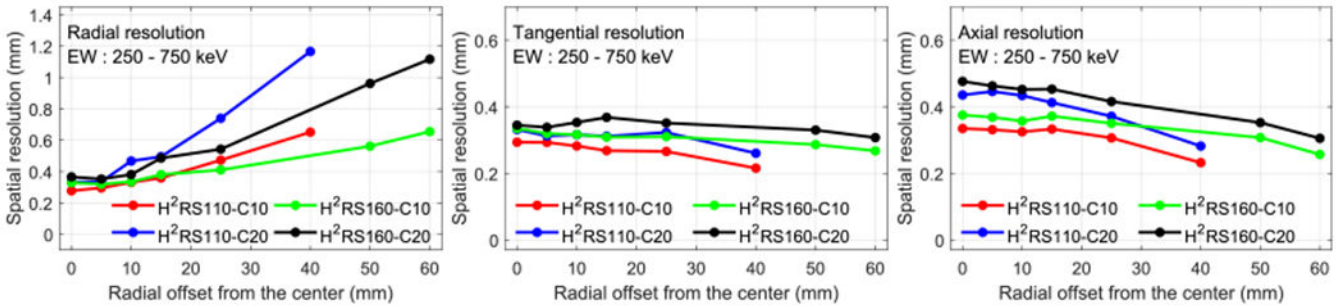

Figure 8.

Radial (left column), tangential (middle column) and axial (right column) resolution versus radial offset with realistic DOI resolutions. A 250–750 keV energy window was used to select events. The DOI resolution for H^2RS110-C10 PET and H^2RS160-C10 PET was 1 mm, and it was 2 mm for H^2RS110-C20 PET and H^2RS160-C20 PET.

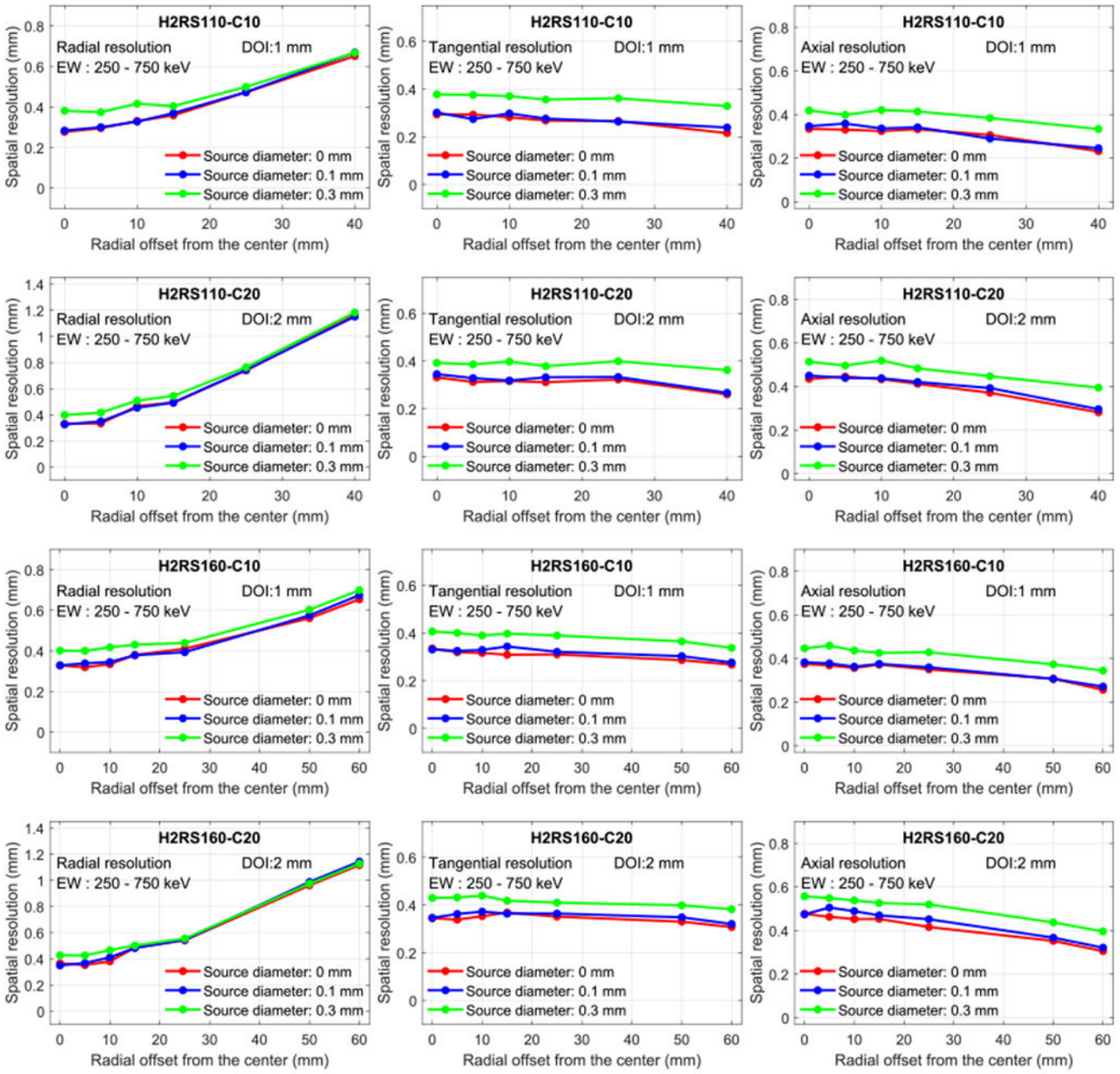

Figure 9.

Effect of the radiation point source size on the resolution. H^2RS110-C10 PET and H^2RS160-C10 PET have a DOI resolution of 1 mm, and H^2RS110-C20 PET and H^2RS160-C20 PET have a DOI resolution of 2 mm.

Table 1.

Characteristics of the four small-animal PET scanners.

	H²RS110-C10 PET	**H²RS110-C20 PET**	**H²RS160-C10 PET**	**H²RS160-C20 PET**
Crystal material	LYSO			
Ring diameter (mm)	110		160	
Axial length (mm)	167		254	
Solid angle (4π)[a]	0.84		0.85	
Crystal size (mm^3)	0.44 × 0.44 × 10	0.44 × 0.44 × 20	0.44 × 0.44 × 10	0.44 × 0.44 × 20
Crystal pitch (mm)	0.5			
Crystal array size	40 × 40		60 × 60	
Detectors per ring	16			
Num. of detector ring	8			
Transaxial FOV (mm)	80		120	
Axial FOV (mm)	167		254	

[a]The solid angle is the one subtended from the center of the FOV. The solid angles of the gaps between detector modules were not subtracted.

Table 2.

Positions for sensitivity studies.

	H^2RS110-C10 PET	H^2RS110-C20 PET	H^2RS160-C10 PET	H^2RS160-C20 PET
Radial offset from center (mm)	0, 5, 10, 15, 25, and 40		0, 5, 10, 15, 25, 50 and 60	
Axial offset from center (mm)	From 0 to 80, with steps of 10		From 0 to 120, with steps of 10	

Table 3.

Positions and DOI resolutions for resolution simulation.

	H²RS110-C10 PET	H²RS110-C20 PET	H²RS160-C10 PET	H²RS160-C20 PET
Radial offset from center (mm)	0, 5, 10, 15, 25, and 40		0, 5, 10, 15, 25, 50 and 60	
Axial offset from center (mm)	0 and ¼ offset		0 and ¼ offset	
DOI resolution (mm)	0, 0.5, 1, 2 and 3			
Source diameter (mm)	0, 0.1 and 0.3			